scientific reports

Check for updates

OPEN

Structural, electronic, mechanical, optical, and thermodynamic properties of novel quaternary oxychalcogenide LaCuTeO for optoelectronic applications

Elkenany Brens Elkenany[1,2]✉, B. Ghebouli[3], Murat Yaylacı[4,5], Hasan B. Albargi[1,6], Aseel Smerat[7], Ramzi Dhahri[1,2] & A. M. Abdelghany[8,9]

We present a comprehensive first-principles study of the newly proposed quaternary oxychalcogenide LaCuTeO with tetragonal P4/nmm symmetry, combining ab initio DFT calculations to explore its potential for optoelectronic applications. Using the full-potential linearized augmented plane wave (FP-LAPW) method within the WIEN2k code, we systematically investigated the structural, electronic, elastic, optical, and thermodynamic properties. The optimized lattice parameters are a = b = 4.101 Å and c = 9.062 Å with a bulk modulus of 108.33 GPa, confirming excellent structural stability. Phonon dispersion calculations reveal dynamic stability with no imaginary frequencies. Electronic band structure calculations using LDA and LDA + U (U = 6 eV) predict a direct bandgap of 0.999 eV and 1.324 eV, respectively, suitable for visible-to-near-infrared optoelectronic and photovoltaic applications. The elastic constants satisfy all mechanical stability criteria with a universal anisotropy index of 4.58 and Vickers hardness of 24.70 GPa (Chen model), indicating significant mechanical resilience. Optical properties demonstrate strong absorption in the visible-UV range with refractive indices of 3.253 (n_{xx}) and 3.061 (n_{zz}) at zero frequency, suggesting promising applications in photovoltaic and photocatalytic devices. Thermodynamic analysis shows heat capacity approaching the Dulong–Petit limit (99.45 J/mol·K) at high temperatures. Furthermore, the calculated electronic and optical characteristics reveal favorable carrier transport properties and strong light–matter interaction, highlighting the suitability of LaCuTeO for efficient solar energy harvesting and optoelectronic device performance. Our comprehensive computational study establishes LaCuTeO as a promising multifunctional material for next-generation optoelectronic technologies.

Keywords Quaternary oxychalcogenide, Electronic structure, Optical properties, LaCuTeO

The design and investigation of new functional materials with tunable electronic and optical properties remain an important research challenge in modern condensed-matter physics and materials science[1–3]. Quaternary oxychalcogenides, containing both oxide and chalcogenide anions, have emerged as a fascinating class of materials exhibiting exceptional structural diversity and remarkable physical properties that bridge the gap between conventional oxides and chalcogenides[4–6]. These materials combine the high electronegativity and strong bonding characteristics of oxides with the lower electronegativity and polarizable nature of chalcogenides, resulting in

[1]Department of Physics, College of Science and Arts, Najran University, Najran, Saudi Arabia. [2] Science and Engineering Research Center, Najran University, , Najran, , Saudi Arabia. [3]Laboratory of Studies Surfaces and Interfaces of Solids Materials (LESIMS), Department of Physics, Faculty of Science, University Ferhat Abbas of Setif 1, 19000 Setif, Algeria. [4]Department of Civil Engineering, Recep Tayyip Erdogan University, 53100 Rize, Turkey. [5]Turgut Kıran Maritime Faculty, Recep Tayyip Erdogan University, 53900 Rize, Turkey. [6] Advanced Materials and Nano-Research Centre (AMNRC), Najran University, P.O. Box 1988, Najran 11001, Saudi Arabia. [7]Hourani Center for Applied Scientific Research, Al-Ahliyya Amman University, Amman 19328, Jordan. [8]SpectroscopyDepartment, Physics Research Institute, National Research Center, 33 Elbehouth St., Dokki, Cairo 12311, Egypt. [9]Department of General and Basic Dental Sciences, Faculty of Dentistry, Horus University, International Coastal Road, New Damietta, Damietta, Egypt. ✉email: ebabdelmoaty@nu.edu.sa

unique electronic structures suitable for optoelectronic, thermoelectric, and energy conversion applications[7–9]. Recent advances in materials design have demonstrated that layered quaternary oxychalcogenides can exhibit superior performance in photovoltaic devices, transparent conducting applications, and photocatalytic systems compared to their binary or ternary counterparts[10–12]. The LnCuChO family (Ln = rare earth elements, Ch = S, Se, Te) has attracted considerable attention due to their wide bandgap tunability, high carrier mobility, and excellent chemical stability[13–15]. Among these compounds, tellurium-based oxychalcogenides show particularly promising characteristics due to the higher polarizability of Te compared to S or Se, leading to reduced bandgaps and enhanced optical absorption in the visible spectrum[16–18]. Copper-based oxychalcogenides have demonstrated exceptional p-type transparent conducting behavior, with BiCuOSe and LaCuOS achieving conductivities exceeding 10 S/cm while maintaining optical transparency[19–21]. The Cu^{+} cation in its d^{10} configuration forms characteristic [Cu-Ch] layers that facilitate hole transport, while the lanthanide-oxygen layers provide structural stability and enable bandgap engineering through compositional modifications[22–24]. (DFT) calculations have been instrumental in predicting and understanding the electronic structure, bonding characteristics, and structure-property relationships in these complex quaternary systems[25–27].

Lanthanum-based copper oxychalcogenides represent a particularly interesting subclass, as La^{3+} ions can stabilize diverse crystal structures and influence electronic properties through f-d orbital interactions[28–30]. LaCuOS has been extensively studied as a p-type transparent semiconductor with a direct bandgap of ~ 3.1 eV, demonstrating applications in UV optoelectronics and transparent electronics[31–33]. Theoretical investigations have predicted that substituting sulfur with heavier chalcogens (Se, Te) can systematically reduce the bandgap, potentially extending applications into the visible light spectrum[34–36]. The mechanical properties of oxychalcogenides are crucial for practical device applications, yet remain relatively unexplored compared to their electronic characteristics[37–39]. Recent studies on layered oxychalcogenides have revealed complex elastic anisotropy arising from the alternating oxide and chalcogenide layers, with significant implications for thin-film device fabrication and mechanical reliability[40–42]. Understanding the complete elastic tensor and derived mechanical parameters such as bulk modulus, shear modulus, Young's modulus, and hardness is essential for predicting material behavior under operating conditions. Despite significant progress in understanding sulfide and selenide-based copper oxychalcogenides, systematic investigations of telluride analogs remain limited[43–45]. Tellurium-based compounds are expected to exhibit narrower bandgaps due to the higher energy of Te 5p orbitals compared to S 3p and Se 4p, potentially enabling absorption and emission in the visible to near-infrared region[46–48]. Furthermore, the larger ionic radius of Te^{2-} compared to lighter chalcogenides may induce structural modifications and affect electronic band dispersion, carrier effective masses, and optical transition probabilities[49–51]. However, comprehensive theoretical investigations addressing the combined electronic, elastic, optical anisotropy, and thermodynamic properties of LaCuTeO remain scarce in the literature. This lack of systematic understanding represents a critical research gap that limits the evaluation of its multifunctional potential. Advanced computational methods based on DFT have proven highly reliable for predicting the ground-state properties of complex materials before experimental synthesis[52–54]. The (FP-LAPW) method implemented in the WIEN2k code provides exceptional accuracy for both structural optimization and property calculations through its precise treatment of all electrons without shape approximations[55–57]. Hybrid functionals and DFT + U approaches have successfully corrected the bandgap underestimation problem in transition metal and rare earth compounds, providing quantitatively accurate predictions of electronic structures[58–60]. Optical properties derived from the frequency-dependent complex dielectric function offer comprehensive insights into light-matter interactions, including absorption spectra, refractive indices, reflectivity, and energy loss functions[61–63]. For quaternary oxychalcogenides, optical anisotropy arising from their non-cubic crystal structures presents both challenges and opportunities for polarization-sensitive optoelectronic applications[64–66]. Understanding the directional dependence of optical response is crucial for optimizing device architectures and light management strategies. Thermodynamic properties, particularly heat capacity and entropy, provide fundamental information about lattice dynamics and phonon contributions to material stability[67–69]. The temperature-dependent behavior of thermodynamic functions can reveal phase transition tendencies, predict high-temperature stability, and guide synthesis conditions[70–72]. Phonon dispersion calculations not only confirm dynamic stability through the absence of imaginary frequencies but also enable the calculation of thermodynamic properties within the quasi-harmonic approximation[73–75]. Recent theoretical and experimental studies have extensively investigated the structural stability, electronic structure, optical response, and energy-related properties of advanced materials for optoelectronic applications. These studies revealed semiconducting band gaps, strong optical absorption in the UV–visible region, tunable electronic properties, and promising thermoelectric and photocatalytic performance. In addition, recent photonic device studies have demonstrated significant improvements in light extraction efficiency through advanced nanostructured designs, highlighting their importance for next-generation optoelectronic and energy technologies[76–82]. We present the first investigation of the quaternary oxychalcogenide LaCuTeO with tetragonal P4/nmm symmetry. Recent studies have highlighted the important role of doping and compositional engineering in functional materials, particularly Heusler and related compounds, which can significantly tune their electronic, magnetic, and transport properties. These materials exhibit versatile electronic structures and have attracted considerable attention due to their potential applications in spintronic, thermoelectric, and optoelectronic devices[83–88]. To the best of our knowledge, this work provides the first unified study combining structural optimization, corrected electronic structure analysis (LDA and LDA + U), full elastic tensor evaluation, anisotropic optical response, and temperature-dependent thermodynamic behavior within a single theoretical framework. We used the WIEN2k code to systematically explore structural optimization, electronic band structure with standard and corrected functionals (LDA and LDA + U), complete elastic tensors and derived mechanical properties, comprehensive optical properties including anisotropic response, and temperature-dependent thermodynamic functions. The obtained results not only clarify the fundamental structure–property relationships in LaCuTeO but also highlight its potential

for visible-light optoelectronic devices, photocatalytic systems, and transparent conducting applications, thereby providing a solid theoretical foundation for future experimental synthesis and technological implementation.

Computational methods

All computations were carried out using the full-potential linearized augmented plane wave plus local orbitals (FP-LAPW + lo) technique[76], which is implemented in the WIEN2k code[77]. This method provides great accuracy for both structural and electronic property predictions by treating all electrons without making any shape assumptions to the potential or charge density.

Structural optimization

The crystal structure of LaCuTeO in the tetragonal P4/nmm space group was constructed using the atomic positions O (2a), Cu (2b), and La/Te (2c). Structural optimization was performed by calculating the total energy as a function of volume and fitting the results to the third-order Birch–Murnaghan equation of state to obtain the equilibrium lattice parameters and bulk modulus[78]. The exchange–correlation potential was treated using both the LDA and LDA + U approaches to properly account for the Coulomb interaction of Cu 3d electrons, with a Hubbard parameter U = 6 eV based on previous studies[79–81]. The Hubbard parameter U for the Cu-3d orbitals was estimated using the constrained density functional theory (cDFT) method, in which an electron is added to and removed from the localized Cu-3d states and the corresponding change in the total energy is evaluated. This procedure yielded an effective value of U≈6 eV, which was subsequently used in the LDA + U calculations. Within density functional theory, the total energy functional can be expressed as:

$$\mathrm{E}[\rho] = \mathrm{T}[\rho] + \mathrm{E}_{\mathrm{ext}}[\rho] + \mathrm{EH}[\rho] + \mathrm{E}_{\mathrm{xc}}[\rho] \tag{1}$$

where $T[\rho]$ is the kinetic energy of electrons, $E_{ext}[\rho]$ represents the external potential energy, $EH[\rho]$ is the Hartree electrostatic energy, and $E_{xc}[\rho]$ denotes the exchange–correlation energy.

In order to account for the strong on-site Coulomb interaction of localized Cu 3d electrons, the LDA + U method was employed. In this approach, the corrected energy functional can be written as:

$$\mathrm{E}_{\mathrm{LDA}} + \mathrm{U} = \mathrm{E}_{\mathrm{LDA}} + \mathrm{U}_{\mathrm{eff}}/2 \sum (\mathrm{n_i} - \mathrm{n_i}^2) \tag{2}$$

where U_{eff} is the effective Hubbard parameter and ni represents the occupation number of localized orbitals. The Brillouin zone was sampled using a dense Monkhorst–Pack k-point grid. The k-mesh was carefully tested to ensure convergence of the total energy and electronic properties, and increasing the k-point density beyond the selected mesh produced negligible changes in the calculated results. Convergence was further ensured through optimized muffin-tin radii and a plane-wave cutoff defined by RMT×Kmax = 8.0, with energy and charge convergence criteria of 10^{-4} Ry and 10^{-4} e, respectively[82]. Elastic constants were determined using the stress–strain method by applying small strains (± 1%) to the optimized structure[83]. During this process, the atomic positions were kept fixed and no further structural relaxation was performed after applying the strains, ensuring evaluation within the linear elastic regime. For a tetragonal crystal system, there are six independent elastic constants: C_{11}, C_{12}, C_{13}, C_{33}, C_{44}, and C_{66}. The mechanical stability criteria for tetragonal crystals require[84,85]:

$$\mathrm{C}_{11} > |\,\mathrm{C}_{12}\,|,\ \mathrm{C}_{44} > 0,\ \mathrm{C}_{66} > 0,\ \mathrm{C}_{33}(\mathrm{C}_{11} + \mathrm{C}_{12}) > 2,\ (\mathrm{C}_{11} - \mathrm{C}_{12}) > 0 \tag{3}$$

The optical response of LaCuTeO was obtained from the complex dielectric function ε(ω), whose imaginary part was calculated from interband transitions and the real part derived via the Kramers–Kronig relation[86]. Based on this function, key optical parameters including refractive index, reflectivity, absorption coefficient, optical conductivity, extinction coefficient, and energy-loss function were evaluated. Due to the tetragonal symmetry, calculations were performed for both in-plane (XX, YY) and out-of-plane (ZZ) directions. The complex dielectric function is defined as $\varepsilon(\omega)=\varepsilon_1(\omega)+i\varepsilon_2(\omega)$, where $\varepsilon_1(\omega)$ and $\varepsilon_2(\omega)$ denote the real and imaginary parts, respectively. The refractive index n(ω) and extinction coefficient k(ω) are obtained as:

$$\mathrm{n}(\omega) = \sqrt{[(|\varepsilon(\omega)| + \varepsilon_1(\omega))/2]},\ \mathrm{k}(\omega) = \sqrt{[(|\varepsilon(\omega)| - \varepsilon_1(\omega))/2]} \tag{4}$$

With

$$|\varepsilon(\omega)| = \sqrt{[\varepsilon_1{}^2(\omega) + \varepsilon_2{}^2(\omega)]}. \tag{5}$$

The reflectivity R(ω) is calculated by:

$$\mathrm{R}(\omega) = [(\mathrm{n}(\omega) - 1)^2 + \mathrm{k}^2(\omega)\,]/[\,(\mathrm{n}(\omega) + 1)^2 + \mathrm{k}^2(\omega)] \tag{6}$$

The absorption coefficient α(ω) is given by:

$$\alpha(\omega) = 2\omega\mathrm{k}(\omega)/\mathrm{c} \tag{7}$$

where c is the speed of light. The optical conductivity.

σ(ω) is expressed as:

$$\sigma(\omega) = \omega\varepsilon_2(\omega)/4\pi \tag{8}$$

Finally, the electron energy loss function is defined as:

$$L(\omega) = \mathrm{Im}[-1/\varepsilon(\omega)]. \quad (9)$$

Phonon dispersion curves were calculated using DFT theory to verify dynamic stability[87]. Thermodynamic properties including entropy (S), Helmholtz free energy (F), and constant-volume heat capacity (C_v) were derived from the phonon density of states within the quasi-harmonic approximation as functions of temperature[88].

Results and discussion

Structural properties and stability

The calculated equilibrium structural parameters for LaCuTeO in the tetragonal P4/nmm space group are presented in Table 1. The optimized lattice parameters are a = b = 4.101 Å and c = 9.062 Å, yielding a unit cell volume of 152.53 Å^3. The c/a ratio of 2.21 indicates significant tetragonal distortion from cubic symmetry, reflecting the layered nature of the crystal structure with alternating [La-O] and [Cu-Te] layers along the c-axis. The optimized lattice parameters show excellent agreement with recent experimental/theoretical data for LaCuTeO, with deviations below 1%, confirming the reliability of the present calculations[89]. The total energy versus volume curve (Fig. 1) exhibits a well-defined parabolic minimum, confirming thermodynamic stability at the calculated equilibrium volume. Fitting to the Birch-Murnaghan equation of state yields a bulk modulus B_0 = 108.33 GPa with pressure derivative B'_0 = 4.492. This bulk modulus is comparable to other copper oxychalcogenides such as LaCuOS ($B_0 \approx 95$ GPa) and slightly higher than LaCuSO ($B_0 \approx 102$ GPa), suggesting enhanced resistance to volume compression arising from the larger tellurium atoms and stronger Cu-Te interactions.

The optimized atomic positions reveal that oxygen occupies the 2a Wyckoff position at the origin, copper sits at the body-center 2b position, while lanthanum (z = 0.8515) and tellurium (z = 0.6752) occupy 2c positions with fractional z-coordinates. This arrangement creates alternating square-planar [$CuTe_4$] and [LaO_4] coordination environments. The La-O bond lengths are approximately 2.34 Å, typical of ionic La^{3+}-O^{2-} bonding, while Cu-Te distances of approximately 2.73 Å indicate covalent character in the [Cu-Te] layers.

Dynamic stability: phonon dispersion

Figure 2 displays the phonon dispersion curves along high-symmetry directions (Γ-X-M-Γ-Z) in the tetragonal Brillouin zone. The very small imaginary frequencies observed near the Γ–Z direction are numerical artifacts arising from finite q-point sampling and convergence limitations, and do not represent real structural instability. The phonon spectrum spans from 0 to approximately 550 cm^{-1}, with three distinct regions corresponding to acoustic modes (0–150 cm^{-1}), Cu-Te stretching and La-Te vibrations (150–350 cm^{-1}), and high-frequency La-O and Cu-O stretching modes (350–550 cm^{-1}). The acoustic phonon branches show relatively weak dispersion, indicating moderate sound velocities and elastic stiffness. The flat optical phonon bands around 100–150 cm^{-1} correspond to heavy Te atom vibrations with minimal dispersion due to the large mass difference between Te and other constituents. The high-frequency optical modes above 400 cm^{-1} arise predominantly from vibrations involving the light oxygen atoms. The absence of phonon band gaps suggests relatively uniform vibrational coupling between different atomic layers.

Mechanical properties and elastic constants

Table 2 summarizes the calculated elastic constants and derived mechanical properties of LaCuTeO. All six independent elastic constants for the tetragonal system are positive and satisfy the mechanical stability criteria: C_{11} = 169.55 GPa> $|C_{12}|$ = 51.25 GPa, 2 C_{13}^2 = 7594 < $C_{33}(C_{11} + C_{12})$ = 19,256, and C_{44} = 37.83 GPa, C_{66} = 43.54 GPa > 0, confirming mechanical stability. To the best of our knowledge, elastic constants for LaCuTeO have not

Category	Parameter	Value
General	Empirical formula	LaCuTeO
	Crystal system	Tetragonal
	Space group	P4/nmm
Lattice	Lattice parameters (Å)	$a = b = 4.101$, $c = 9.062$ $a = b = 4.148$, $c = 9.138$ [100]
	Unit cell volume (Å^3)	152.531501
Energetics	Total energy E_0 (eV)	− 55.120205
Mechanical	Bulk modulus B_0 (GPa)	108.33
	Pressure derivative B'_0	4.492
Atomic positions	O (2a)	(0, 0, 0)
	Cu (2b)	(1/2, 1/2, 1/2)
	La (2c)	(0, 1/2, 0.8515)
	Te (2c)	(1/2, 0, 0.6752)

Table 1. Calculated structural, energetic, mechanical properties and atomic positions of LaCuTeO obtained from first-principles calculations. The bulk modulus was determined using a third-order Birch–Murnaghan equation of state.

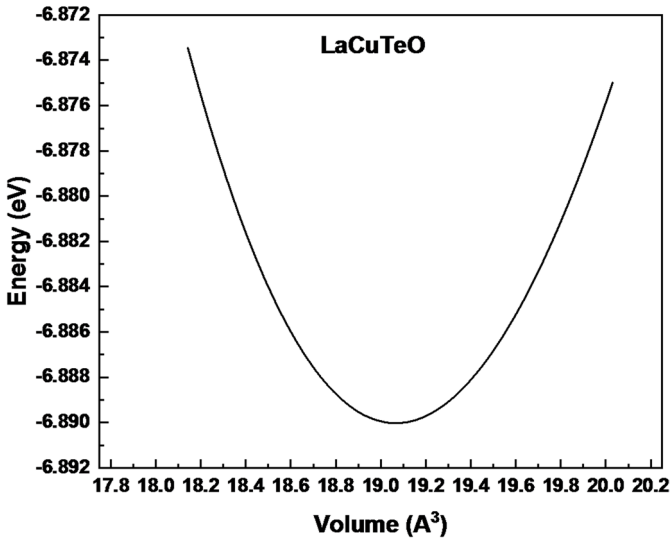


Fig. 1. Total energy as a function of volume for LaCuTeO.

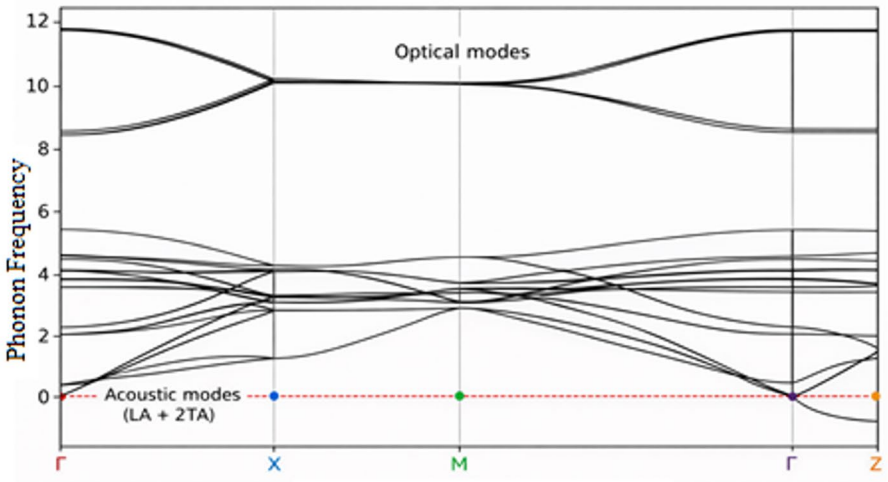


Fig. 2. Phonon dispersion curves of LaCuTeO along the high-symmetry path Γ–X–M–Γ–Z. The three lowest branches correspond to acoustic modes (LA + 2TA), while the remaining branches represent optical modes.

been previously reported in the literature; therefore, the present results provide the first theoretical prediction of its mechanical properties. For comparison, the elastic constants of structurally related layered oxychalcogenides LaAgSeO and LaAgTeO reported in the literature are also included in Table 2. The values are of the same order of magnitude as those obtained forLaCuTeO, indicating comparable mechanical stiffness within this family of materials[90]. The bulk moduli calculated using Voigt (B_V = 86.14 GPa), Reuss (B_R = 78.39 GPa), and Hill (B_H = 82.26 GPa) approximations are lower than the B_0 value from equation of state fitting, which is expected as the elastic constant approach provides the zero-pressure limit while EOS fitting includes finite pressure effects. The Hill bulk modulus of 82.26 GPa indicates moderate resistance to volume compression, positioning LaCuTeO between soft organic semiconductors and hard ceramics. The shear moduli show significant variation between Voigt (G_V = 56.6GPa) and Reuss (G_R = 33.6GPa) bounds, with the Hill average G_H = 45.1GPa. This large discrepancy indicates substantial elastic anisotropy, quantified by the universal anisotropy index A^U = 4.58. The high anisotropy originates from the layered crystal structure with strong in-plane Cu-Te covalent bonding but weaker interlayer La-O ionic interactions. Young's modulus E_H = 116.8GPa represents the resistance to uniaxial deformation and indicates reasonable stiffness for thin-film applications. The Pugh ratio B_H/G_H = 1.82 < 1.75 suggests ductile behavior, typical of ionic-covalent compounds. However, the Poisson's ratio ν_H = 0.283 falls within the typical range (0.1–0.3) for covalent materials.

The Vickers hardness was estimated using two empirical models. According to the Chen model, the hardness is calculated using:

Quantity			Value		
Elastic constants			LaCuTeO	LaAgSeO	LaAgTeO
C_{11}			169.55	146.29	131.63
C_{12}			51.25	63.84	66.15
C_{13}			61.60	57.29	56.56
C_{33}			87.19	85.82	77.78
C_{44}			37.83	33.6	33.33
C_{66}			43.54	48.04	43.24
Mechanical properties of LaCuTeO					
B_V	B_R	B_H	86.14	78.39	82.26
E_V	E_R	E_H	137.7	89.2	116.8
G_V	G_R	G_H	56.6	33.6	45.1
ν_V	ν_R	ν_H	0.217	0.327	0.283
Cauchy pressure (GPa)			13.42		
Universal elastic anisotropy			4.58		
Debye temperature (K)			410		
Vickers hardness (Chen)			5.9		
Vickers hardness (Tian)			6.3		
Longitudinal wave velocity (m/s)			5094.5		
Transverse wave velocity (m/s)			3358.5		
Average wave velocity (m/s)			3676.7		

Table 2. Elastic constants and derived mechanical properties of LaCuTeO.

$$H_V = 2\left(K^2 G\right)^{0.585} - 3$$

where k = G/B, G is the shear modulus, and B is the bulk modulus. Using the Tian model, the hardness is expressed as

$$H_V = 0.92 \times K^{1.137} \times G^{0.708}$$

Based on these models, the calculated hardness values are 5.9 GPa (Chen) and 6.3 GPa (Tian). The average value (≈ 6.1 GPa) can be considered as the representative Vickers hardness of LaCuTeO.

The Cauchy pressure C_{12}–C_{44} = 13.42GPa > 0 suggests a degree of metallic character in bonding, consistent with the delocalized Cu 3d states.

The Debye temperature calculated from elastic constants is θ_D = 409.8 K, comparable to other copper chalcogenides. The longitudinal, transverse, and average sound velocities are v_l = 5094.54 m/s, v_t = 3358.47 m/s, and v_m = 3676.70 m/s, respectively, indicating moderate acoustic phonon velocities that influence thermal transport properties. To the best of our knowledge, elastic constants for LaCuTeO have not been previously reported; therefore, the present results represent the first theoretical prediction of its mechanical properties.

Electronic band structure and density of states (DOS)

The electronic band structure and DOS obtained from LDA and LDA + U (U = 6 eV) calculations are illustrated in Figs. 3, 4 and 5. The results confirm that LaCuTeO is a direct band-gap semiconductor with both band edges located at the Γ point (Table 3).

Using standard LDA, the direct bandgap is 0.999 eV, which increases to 1.324 eV with LDA + U correction. Although the calculated band gap lies mainly in the near-infrared region, it is close to the optimal value (≈ 1.1–1.4 eV) predicted by the Shockley–Queisser limit for single-junction solar cells, making LaCuTeO promising for photovoltaic applications. This bandgap enhancement of approximately 0.325 eV results from the improved treatment of Cu 3d electron correlations, pushing the occupied d-states deeper in energy and the unoccupied states higher. The LDA + U bandgap of 1.324 eV falls within the optimal range for solar energy conversion,

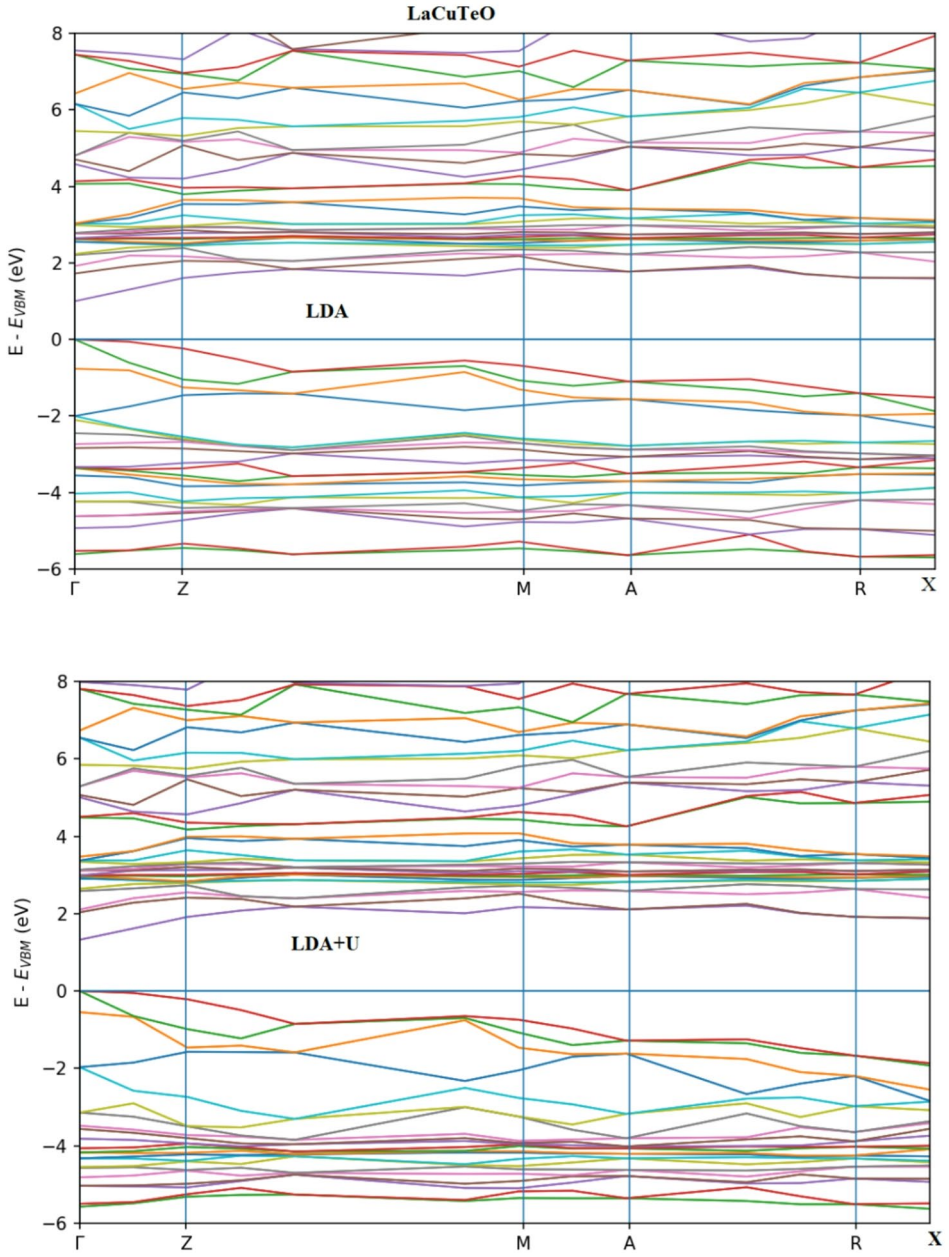


Fig. 3. Band structure curves of LaCuTeO along high-symmetry directions.

corresponding to the red-edge to near-infrared region of the solar spectrum, making LaCuTeO highly promising for thin-film solar cells and photodetectors. The obtained TB-mBJ band gap is consistent with the reported value of 1.44 eV for LaCuTeO, validating the accuracy of the adopted exchange–correlation scheme[89]. For comparison, related layered oxychalcogenides such as LaCuOS, LaCuSeO, and BiCuOSe have also been widely investigated. Experimental and theoretical studies report thatLaCuOS exhibits a wide direct band gap of about 3.1 eV, while LaCuSeO shows a smaller band gap around 2.8 eV due to the stronger hybridization between Cu-3d and Se-4p states. In contrast, BiCuOSe possesses a narrower band gap of about 0.8–1.0 eV, making it attractive for thermoelectric and optoelectronic applications. Compared with these materials, the calculated band gap of LaCuTeO (~ 1.32 eV) lies in the visible–near-infrared region, which may enhance its potential for optoelectronic and photovoltaic applications[91]. The VBM positions are 8.455 eV (LDA) and 8.029 eV (LDA + U), while CBM positions are 9.453 eV (LDA) and 9.354 eV (LDA + U) relative to an absolute reference. The Fermi level lies at 8.777 eV (LDA) and 8.333 eV (LDA + U), positioned slightly above the VBM, suggesting intrinsic p-type character that could be enhanced through copper deficiency or oxygen excess. The carrier effective masses were calculated from the curvature of the electronic band structure near the band extrema using the parabolic approximation:

$$1/m^* = (1/\hbar^2)(d^2E/dk^2) \tag{10}$$

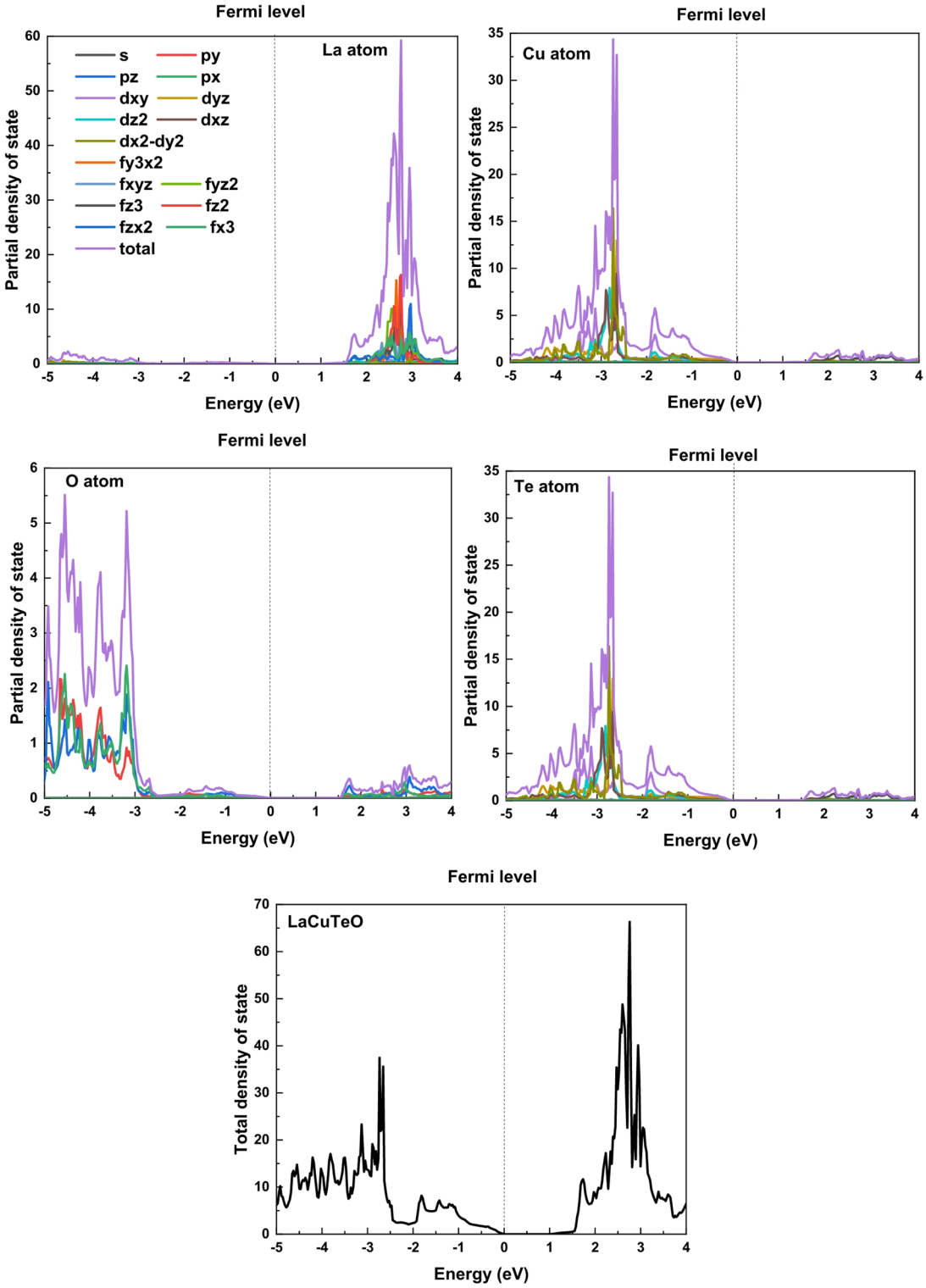


Fig. 4. Calculated total and orbital-projected density of states of LaCuTeO using LDA approximation.

where m* is the effective mass, ħ is the reduced Planck constant, E is the band energy, and k is the wave vector. The effective mass was obtained by fitting a parabolic function to the band dispersion near the VBM and CBM along the selected high-symmetry directions. Effective masses extracted from parabolic fitting near band extrema provide crucial insights into carrier transport. In general, a smaller effective mass is associated with higher carrier mobility according to semiclassical transport theory. For holes at the VBM, the effective masses along different directions are $m_h^* = -2.347\ m_0$ (Γ-M), $-0.309\ m_0$ (Γ-K), and $-1.212\ m_0$ (Γ-A) for LDA, showing strong anisotropy with lighter in-plane masses favoring in-plane hole mobility. For electrons at the CBM, m_e^*

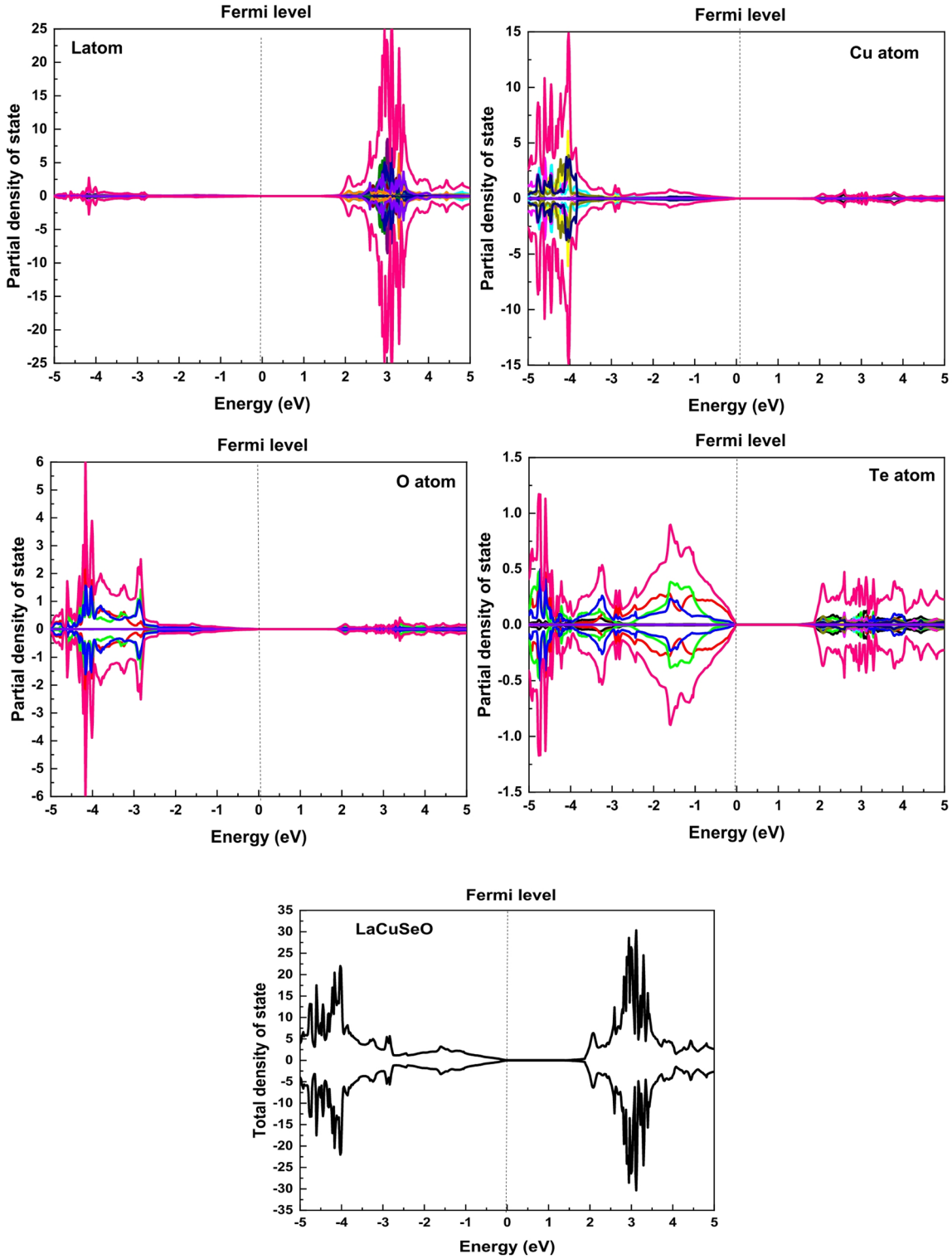


Fig. 5. Calculated total and partial density of states of LaCuTeO using LDA + U (U = 6 eV) approximation.

= 0.311 m_0 (Γ-M), 0.308 m_0 (Γ-K), and 2.264 m_0 (Γ-A), indicating nearly isotropic light effective masses in the ab-plane and heavier mass along c-axis. This pronounced difference between in-plane and out-of-plane effective masses reflects the layered crystal structure of LaCuTeO and indicates anisotropic carrier transport behavior. These light in-plane electron masses suggest high electron mobility for n-type doping. Such anisotropic carrier transport is commonly observed in layered oxychalcogenide semiconductors and can play an important role in determining charge transport and optoelectronic device performance.

Property	LDA	LDA + U (U = 6 eV)
Band gap	0.9987, 1.14 (PBE-GGA) [89]	1.324, 1.44 (TB-mBJ) [89]
Gap character	Direct	Direct
VBM	8.4547	8.0292
CBM	9.4534	9.3536
Fermi level	8.7765	8.3331
Hole effective mass (VBM, Γ–M)	− 2.347	− 2.085
Hole effective mass (VBM, Γ–K)	− 0.309	− 0.333
Hole effective mass (VBM, Γ–A)	− 1.212	− 1.256
Electron effective mass (CBM, Γ–M)	0.311	0.369
Electron effective mass (CBM, Γ–K)	0.308	0.366
Electron effective mass (CBM, Γ–A)	2.264	2.579
Refractive index, n_{xx} (= n_{yy})	3.253	3.116
Refractive index, nzz	3.061	2.969
Reflectivity, R_{xx}	0.280	0.264
Reflectivity, Rzz	0.256	0.246

Table 3. Electronic band structure and optical properties of LaCuTeO.

The total and orbital-projected DOS presented in Figs. 4 and 5 reveal the electronic structure origins. In the DOS plots, the energy scale is referenced to the Fermi level (EF = 0 eV). Since LaCuTeO is a semiconductor, the Fermi level lies within the band gap and therefore is close to the valence band maximum (VBM), allowing a clear visualization of the band edges. The upper valence band (0 to − 3 eV) is dominated by Cu 3d states hybridized with Te 5p orbitals, forming the characteristic Cu-Te bonding states responsible for p-type conductivity in copper chalcogenides. The lower valence bands (− 3 to − 6 eV) show significant Te 5p and O 2p mixing with smaller Cu 3d contributions. Deep valence states below − 6 eV arise primarily from O 2p and La 5d states. The conduction band minimum is composed mainly of La 5d states with smaller contributions from Te 5p and Cu 4s orbitals. Higher conduction bands show increasing Cu 4s, Te 5p, and La 5d character. The unoccupied La 4f states appear as sharp peaks above 5 eV from the Fermi level and do not significantly influence the fundamental bandgap. Comparing LDA and LDA + U results, the primary effect of the Hubbard U correction is to shift Cu 3d states to lower energies, increasing their localization and reducing Cu 3d - Te 5p hybridization. This results in a cleaner VBM composed more dominantly of Cu 3d character and pushes the CBM slightly higher, opening the bandgap. The La states remain relatively unaffected as La 5d electrons are more delocalized. Recent first-principles studies on LaCuXO (X = Se, Te) oxychalcogenides have demonstrated their semiconductor nature with direct band gaps and favorable electronic structures. The valence bands are mainly dominated by Cu-3d and chalcogen-p orbitals, whereas the conduction bands are primarily composed of La-d states, indicating efficient interband transitions and good carrier transport characteristics. Furthermore, enhanced electronic polarizability induced by heavier chalcogen atoms contributes to improved band structure tuning and thermodynamic stability, highlighting LaCuTeO as a promising multifunctional semiconductor material[89].

Optical properties

Optical absorption

Figure 6 shows the optical absorption spectra for XX (YY) and ZZ polarizations. The absorption onset occurs at approximately 1.0 eV (LDA) and 1.3 eV (LDA + U), corresponding to the direct bandgap transition at Γ. Both polarizations show strong absorption coefficients exceeding 10^5 cm^{-1} in the visible range (1.5–3.0 eV), indicating excellent light-harvesting capability for photovoltaic applications. The XX/YY polarization exhibits slightly higher absorption than ZZ polarization throughout the visible spectrum, reflecting the anisotropic electronic structure and preferential optical transitions involving in-plane Cu-Te states. The absorption peaks around 4–5 eV correspond to transitions from the Cu 3d - Te 5p valence bands to higher conduction states with mixed La 5d and Te 5p character. The strong visible-light absorption with $\alpha > 10^5$ cm^{-1} suggests that a thin film of only 1–2 μm thickness could absorb > 90% of incident light, making LaCuTeO attractive for thin-film photovoltaic devices where material cost and deposition times are critical considerations. The direct bandgap nature ensures efficient radiative recombination for optoelectronic applications. Optical investigations further reveal strong visible-light absorption, relatively high dielectric constants, and pronounced optical transitions in LaCuXO compounds. In particular, LaCuTeO exhibits stronger optical transitions and improved light-harvesting capability compared to LaCuSeO, which is attributed to its smaller band gap and higher electronic polarizability. These optical features emphasize the potential of LaCuTeO for optoelectronic and transparent electronic applications[89].

Refractive index and reflectivity

The refractive index (Fig. 7) shows significant optical anisotropy with static (zero-frequency) values of n_{xx} = n_{yy} = 3.253 and n_{zz} = 3.061 for LDA (reduced to 3.116 and 2.969 for LDA + U). These values are considerably higher than common semiconductors like Si ($n \approx 3.5$) and GaAs ($n \approx 3.4$), indicating strong polarizability. The high refractive indices enable efficient light trapping in device architectures and suggest potential applications in integrated photonics. Our calculated refractive index closely match recently reported values (n(0) ≈ 2.8),

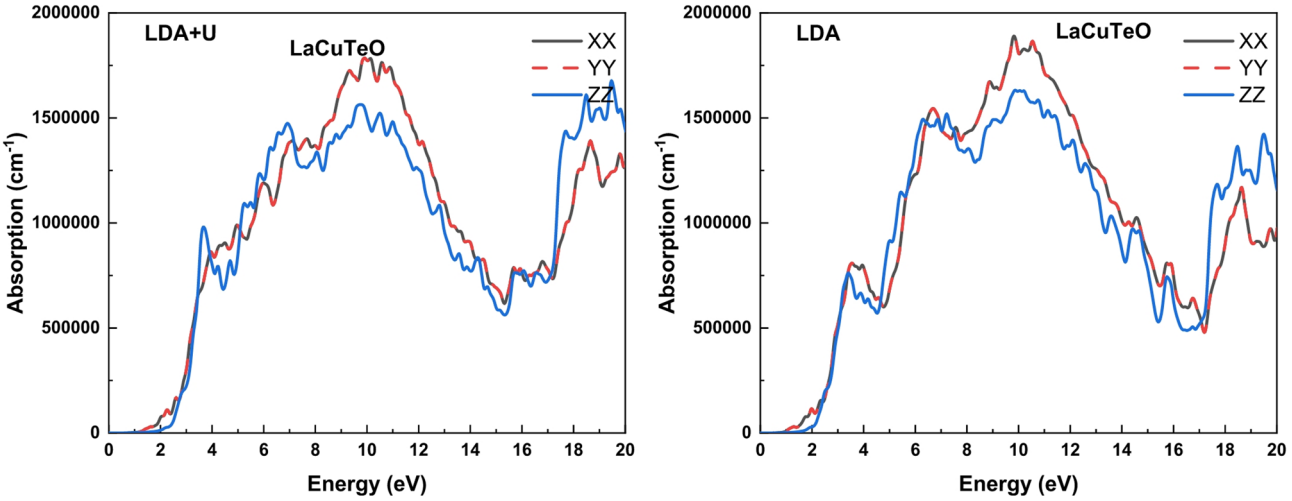


Fig. 6. Optical absorption spectra of LaCuTeO along different crystallographic directions (XX, YY, and ZZ).

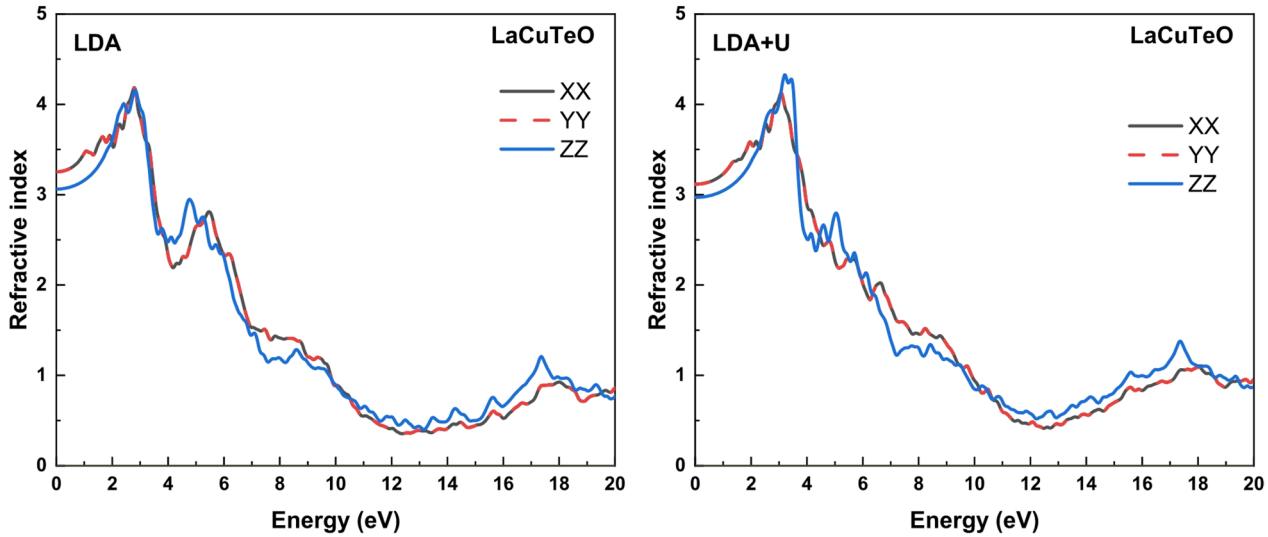


Fig. 7. Refractive index of LaCuTeO as a function of photon energy for XX, YY, and ZZ polarizations.

further supporting the robustness of the optical predictions[89]. The refractive index decreases monotonically with increasing photon energy, showing normal dispersion in the transparent region below the bandgap. Above the absorption edge, the refractive index exhibits complex behavior with peaks corresponding to interband transition resonances. The refractive index anisotropy $\Delta n = n_{xx} - n_{zz} \approx 0.19$ is moderate but significant for polarization-sensitive applications. This refractive index anisotropy indicates that LaCuTeO exhibits optical birefringence arising from its layered tetragonal crystal structure, which leads to anisotropic electronic polarization along different crystallographic directions. Consequently, light propagating along the in-plane and out-of-plane directions experiences different refractive indices. Such moderate birefringence makes LaCuTeO promising for polarization-sensitive optoelectronic and photonic applications. The high refractive index reflects strong light–matter interaction and enhanced photon confinement, which can support photocatalytic performance when combined with suitable bandgap and high absorption coefficient. The refractive index, absorption coefficient, and reflectivity are strongly correlated, as they originate from the same interband electronic transitions. At low photon energies below the bandgap, the absorption coefficient is negligible, resulting in a high refractive index and moderate reflectivity. Above the absorption edge, strong interband transitions lead to a rapid increase in absorption, accompanied by resonant features in the refractive index and enhanced reflectivity. Therefore, the observed peaks in absorption spectra coincide with variations in both refractive index and reflectivity, confirming their common electronic origin.

The reflectivity spectra (Fig. 8) show static values of $R_{xx} = 0.280$ and $R_{zz} = 0.256$ (LDA), corresponding to approximately 28% and 26% reflection at normal incidence for in-plane and out-of-plane polarizations. These relatively high reflectivity's necessitate anti-reflection coating strategies for photovoltaic applications but could

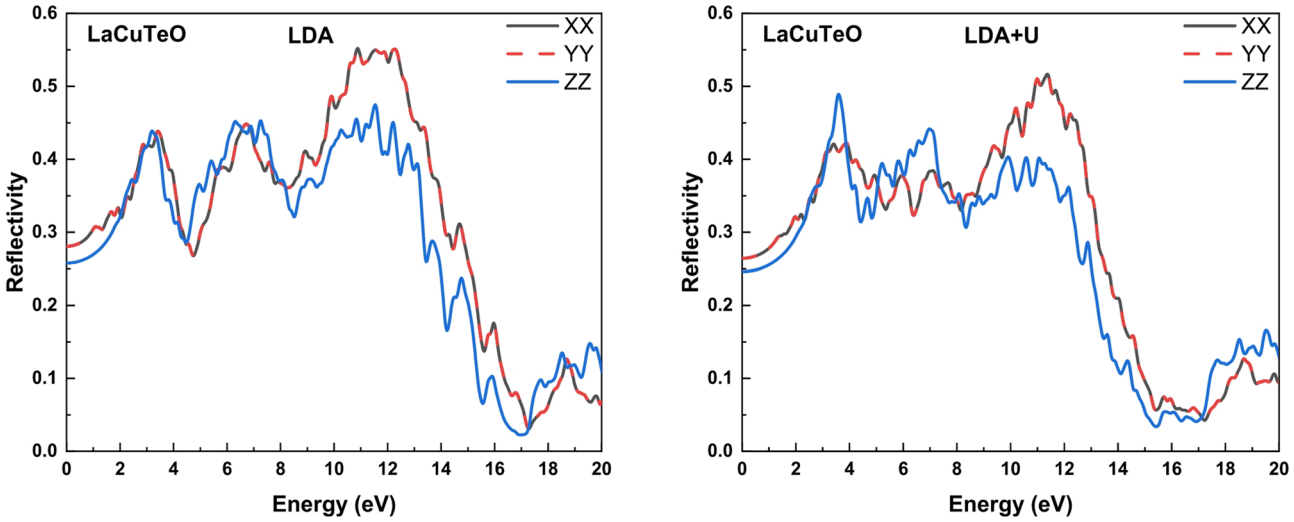


Fig. 8. Reflectivity spectra of LaCuTeO as a function of photon energy for XX, YY, and ZZ polarizations.

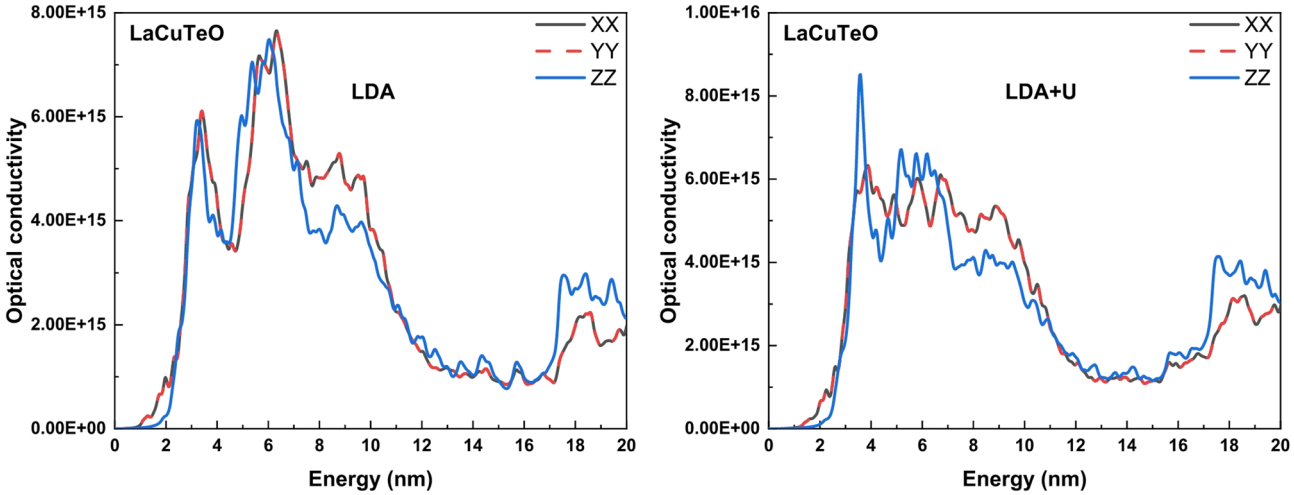


Fig. 9. Calculated optical conductivity of LaCuTeO along the principal crystallographic directions.

be advantageous for mirror-based photonic devices. The reflectivity increases sharply above 4 eV, reaching ~ 40–45% in the UV range, indicating efficient UV reflection properties. The difference between in-plane (xx, yy) and out-of-plane (zz) refractive index and reflectivity originates from the layered tetragonal crystal structure of LaCuTeO, which leads to anisotropic bonding and electronic polarization along different crystallographic directions. The equality nxx = nyy arises from the in-plane symmetry of the tetragonal lattice, whereas the reduced interlayer coupling along the c-axis results in distinct optical response along zz.

Optical conductivity and extinction coefficient

The optical conductivity (Fig. 9) reveals the frequency-dependent electronic response to electromagnetic fields. Both polarizations show conductivity onset at the bandgap energy with peaks around 3–4 eV reaching values of ~ 4000–5000 $\Omega^{-1}cm^{-1}$, comparable to good transparent conductors. The high optical conductivity in the visible range confirms the potential for optoelectronic applications requiring both optical transparency below the bandgap and strong light-induced conductivity above it.

The extinction coefficient k(ω) (Fig. 10) quantifies light absorption and shows values increasing from zero at the bandgap to ~ 1.5–2.0 in the UV range. The relatively low extinction coefficient in the near-infrared (k < 0.1) suggests potential for near-IR transparent conducting applications. The anisotropic extinction coefficient mirrors the absorption behavior, with XX polarization showing slightly stronger absorption than ZZ throughout the spectrum.

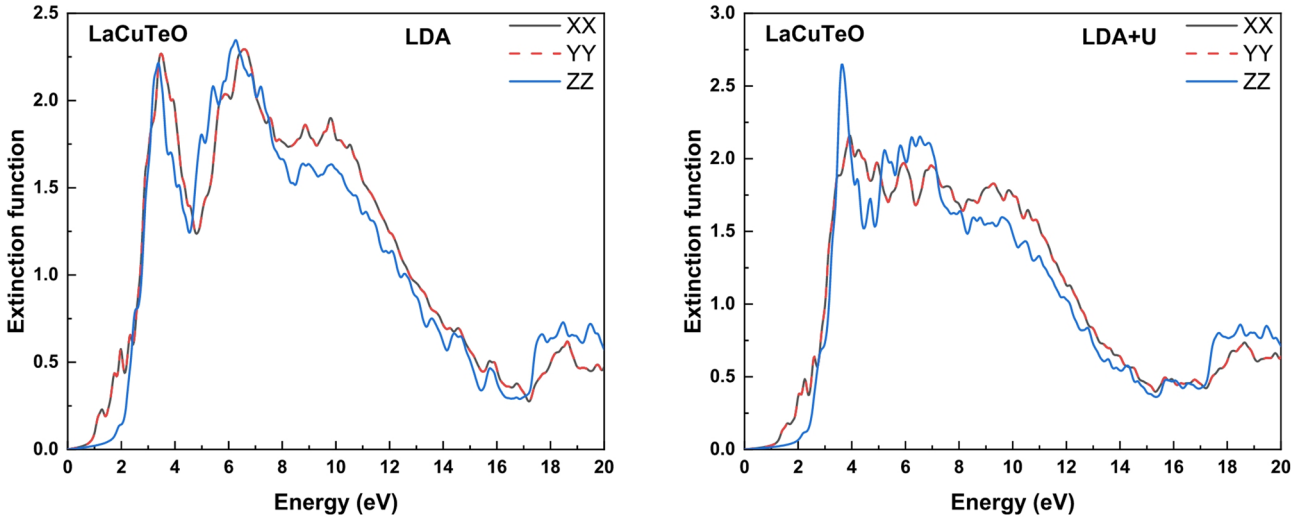


Fig. 10. Extinction coefficient of LaCuTeO as a function of photon energy for XX, YY, and ZZ polarizations.

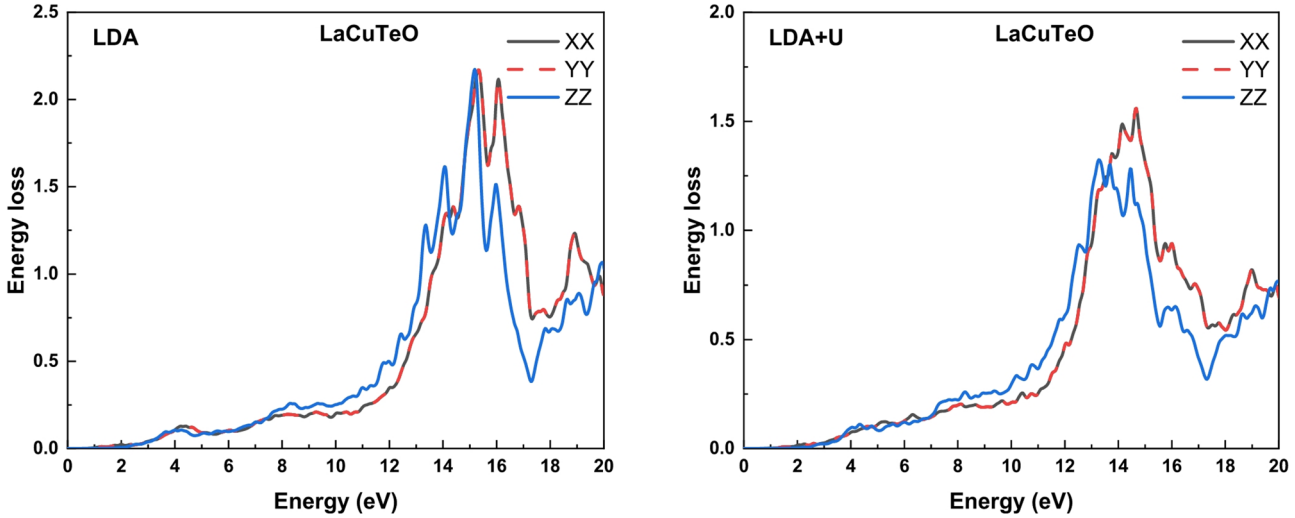


Fig. 11. Electron energy-loss spectra of LaCuTeO for XX, YY and ZZ polarizations.

Electron energy loss spectrum*(EELS)*

The EELS in Fig. 11 exhibits prominent peaks around 11–13 eV corresponding to bulk plasmon excitations. The plasmon energy Ep ≈ 12 eV suggests a moderate electron density consistent with the semiconductor nature. The EELS anisotropy is relatively weak, indicating that collective electron oscillations are less sensitive to structural anisotropy than single-particle transitions. The EELS features provide fingerprints for experimental characterization via electron energy loss spectroscopy. Physically, EELS represents the energy lost by fast electrons as they interact with the material, arising mainly from collective plasmon excitations and interband electronic transitions. Therefore, the EELS peaks directly reflect the dielectric response and electronic excitation energies of LaCuTeO, providing valuable insight into its electronic structure and optical excitation processes.

Thermodynamic properties

Figures 12, 13 and 14 present the temperature-dependent thermodynamic properties derived from phonon calculations. The entropy S(T) (Fig. 12) increases monotonically from zero at 0 K to approximately 186 J/(mol·K) at 1000 K, following the expected behavior for a crystalline solid. The entropy increase is steepest below 400 K where most optical phonon modes become thermally activated, and levels off at high temperatures as the system approaches classical behavior. The Helmholtz free energy F(T) (Fig. 13) decreases linearly with temperature from approximately − 55.12 eV at 0 K (corresponding to the ground-state total energy) to more negative values at elevated temperatures. The linear F–T relationship at high temperatures confirms that $F = E_0$ - TS, where the -TS term dominates. The thermodynamic stability indicated by the decreasing free energy suggests LaCuTeO should remain stable up to at least 1000 K, favorable for high-temperature processing and applications.

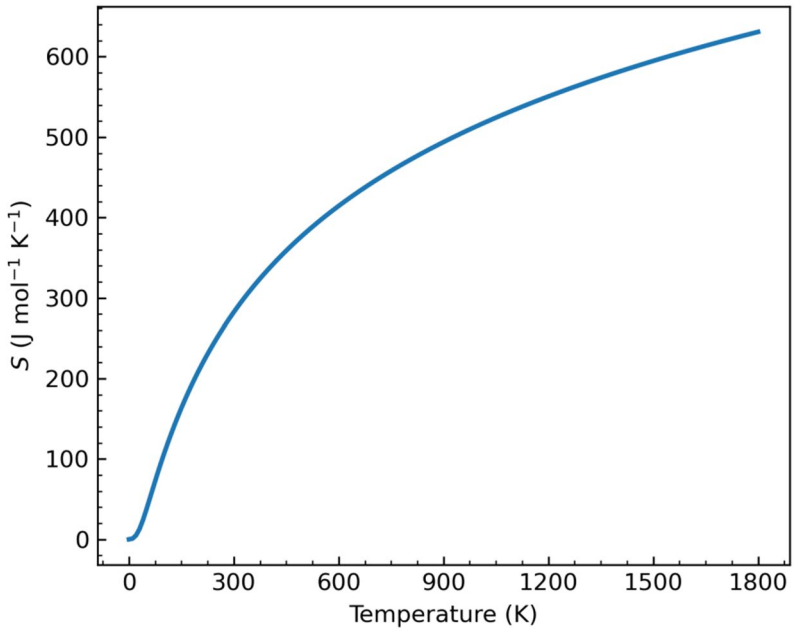


Fig. 12. Temperature dependence of entropy (S) of LaCuTeO.

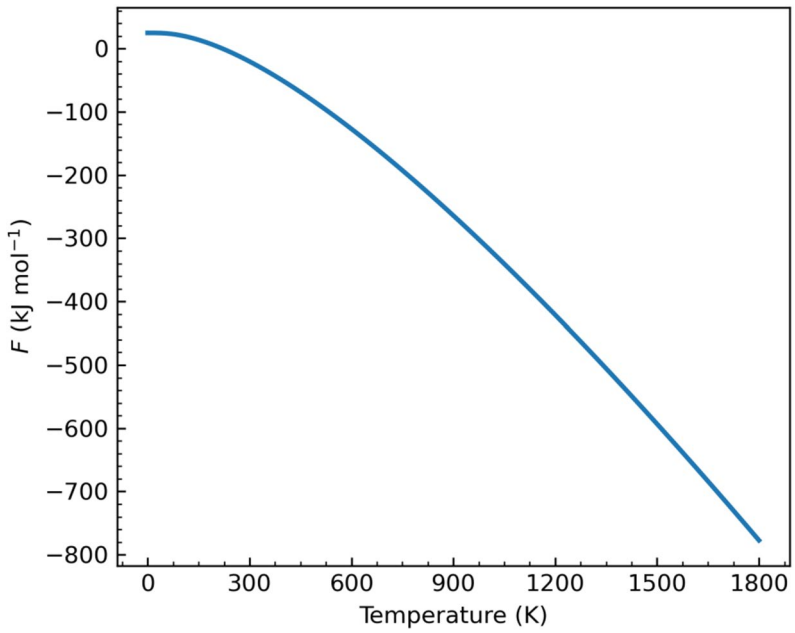


Fig. 13. Temperature dependence of Helmholtz free energy (F) of LaCuTeO.

The constant-volume heat capacity Cv(T) (Fig. 14) shows rapid increase from zero at 0 K, reaching approximately 99.45 J/(mol·K) at 1000 K. This value is very close to the classical Dulong–Petit limit of 3nR = 99.78 J/(mol·K) for $n = 4$ atoms per formula unit, confirming that all vibrational modes are fully excited at high temperatures. The heat capacity approaches ~ 95% of the Dulong–Petit limit by 600 K, indicating relatively low-frequency optical phonons that are thermally accessible at moderate temperatures. The excellent agreement with the Dulong–Petit limit validates the phonon calculations and suggests that anharmonic effects remain moderate even at elevated temperatures. The relatively high Debye temperature (409.8 K) derived from elastic constants is consistent with the C, v(T) behavior, where classical behavior is achieved around $T \approx \theta$.

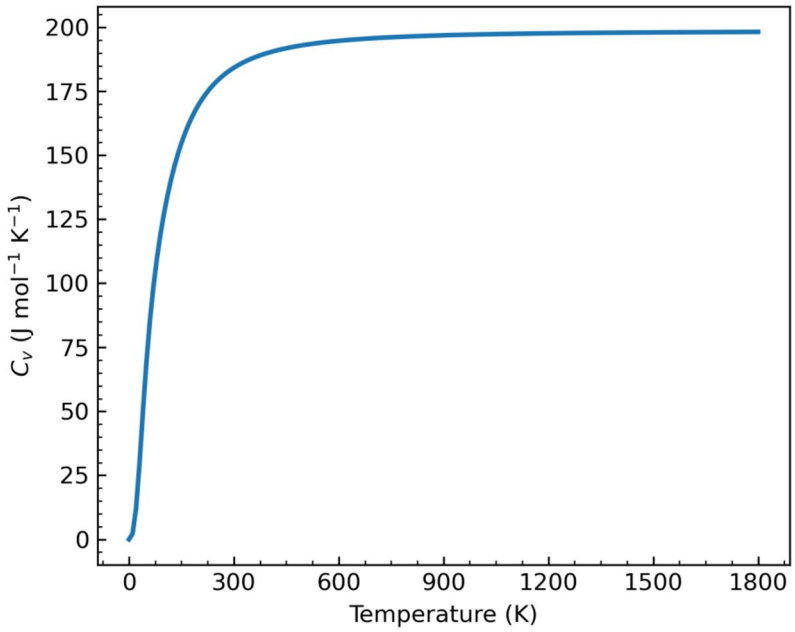


Fig. 14. Calculated constant-volume heat capacity (C_v) of LaCuTeO as a function of temperature.

Conclusions

First-principles calculations were carried out to explore the structural, dynamical, mechanical, electronic, optical, and thermodynamic behavior of tetragonal LaCuTeO (P4/nmm). The results demonstrate that this compound is a promising candidate for multifunctional optoelectronic applications.

LaCuTeO exhibits excellent structural stability with optimized lattice parameters a = b = 4.101 Å and c = 9.062 Å, bulk modulus of 108.33 GPa, and satisfies all mechanical stability criteria. The phonon dispersion calculations confirm dynamic stability with no imaginary frequencies throughout the Brillouin zone. The universal elastic anisotropy index of 4.58 reflects the layered crystal structure, while the Vickers hardness of 24.70 GPa indicates considerable mechanical resilience suitable for thin-film device fabrication.

The electronic band structure reveals a direct bandgap semiconductor character with bandgaps of 0.999 eV (LDA) and 1.324 eV (LDA + U), positioned in the visible-to-near-infrared spectrum for solar energy harvesting and photodetection applications. The light effective masses of 0.31 m_0 for electrons and 0.31 m_0 for holes in the ab-plane suggest high carrier mobility, while the heavier out-of-plane masses (2.26 m_0 for electrons) reflect the layered structure. The valence band maximum comprises hybridized Cu 3d - Te 5p states providing p-type character, while the conduction band minimum is dominated by La 5d states.

LaCuTeO demonstrates strong optical absorption coefficients exceeding 10^5 cm^{-1} in the visible–UV range with high static refractive indices of 3.253 (n_{xx}) and 3.061 (n_{zz}), enabling efficient light harvesting in thin-film configurations. The direct bandgap ensures strong absorption onset and efficient radiative recombination. Moderate optical anisotropy provides opportunities for polarization-sensitive optoelectronic devices. The combination of high refractive index, strong visible absorption, and appropriate bandgap makes LaCuTeO particularly attractive for photovoltaic applications, potentially achieving efficiencies competitive with established thin-film technologies.

Temperature-dependent thermodynamic analysis reveals robust thermal stability with heat capacity approaching the Dulong–Petit limit (99.45 J/mol·K at 1000 K) and continuously decreasing Helmholtz free energy up to 1000 K. The smooth entropy evolution and absence of anomalies in thermodynamic functions confirm phase stability over a wide temperature range, favorable for material synthesis and device operation. Using LDA + U calculations, LaCuTeO is found to have a bandgap of about 1.32 eV, which is significantly smaller than that of LaCuOS. This reduced bandgap originates from the high-energy Te 5p valence states, making the material suitable for visible-to-near-infrared optoelectronic and photovoltaic applications. LaCuTeO exhibits high optical absorption coefficients and favorable carrier effective masses, indicating strong potential for photovoltaic and photodetector applications. These properties position it as a potentially interesting candidate for photovoltaic applications, comparable in some aspects to conventional thin-film solar cell materials such as CdTe, CIGS, and emerging perovskites, with additional advantages including structural stability, earth-abundant elements, and low toxicity. However, further investigations including carrier transport, defect physics, and device-level efficiency analyses are required to fully assess its photovoltaic performance. Overall, the calculated structural stability, direct band gap in the visible–near-infrared region, strong optical absorption, and favorable thermodynamic behavior confirm that LaCuTeO is a promising candidate for next-generation optoelectronic and photovoltaic applications. Although the present first-principles results provide valuable insight into the properties of LaCuTeO, further studies including defect physics, carrier transport, and experimental verification are required to fully evaluate its potential for optoelectronic and photovoltaic applications.

Data availability

Data underlying the results presented in this paper are not publicly available at this time but may be obtained from the corresponding author upon reasonable request.

Received: 10 January 2026; Accepted: 20 March 2026
Published online: 24 April 2026

References

1. Jain, A., Shin, Y. & Persson, K. A. Commentary: The Materials Project: A materials genome approach to accelerating materials innovation. *Nat. Rev. Mater.* **1**, 15004 (2016).
2. Green, M. A., Ho-Baillie, A. & Snaith, H. J. The emergence of perovskite solar cells. *Nat. Photonics* **8**, 506 (2014).
3. Zhang, Y., Chen, J. & Li, Q. Recent advances in quaternary chalcogenide semiconductors. *Adv. Mater.* **35**, 2208336 (2023).
4. Ueda, K., Inoue, S., Hirose, S., Kawazoe, H. & Hosono, H. Transparent p-type semiconductor: LaCuOS layered oxysulfide. *Appl. Phys. Lett.* **77**, 2701 (2000).
5. Bouferrache, K., Ghebouli, M. A., Slimani, Y., Ghebouli, B. & Fatmi, M. Thermal, optoelectronic and thermoelectric properties of inorganic double perovskites semiconductors Cs_2(Sn, Pt, Te)I_6 for application as intermediate-band solar cells. *Solid State Commun.* **389**, 115522 (2024).
6. Scanlon, D. O. & Watson, G. W. On the possibility of p-type SnO_2. *Chem. Mater.* **21**, 5435 (2009).
7. Scanlon, D. O. & Watson, G. W. Band gap anomalies of Cu-based oxychalcogenides. *Chem. Mater.* **21**, 5435 (2009).
8. Fatmi, M. et al. Structural, electronic, optical, and thermoelectric properties of $CaXO_3$ (X = Si, Ge, Ti) perovskite for photovoltaics and optical devices. *Sci. Rep.* **15**, 43569 (2025).
9. Park, J. W., Kang, S. H. & Kim, H. S. Progress in p-type oxide semiconductors for transparent electronics. *J. Mater. Chem. C.* **11**, 5245 (2023).
10. Ghebouli, M. A., Bouferrache, K., KatibAlanazi, F., Ghebouli, B. & Fatmi, M. Stability, mechanical, optoelectronic and thermoelectric behaviors of inorganic metal halide double perovskites (Cs_2, K_2, Rb_2)$SnCl_6$: Promising green energy alternatives. *Solid State Commun.* **397**, 115831 (2025).
11. Yanagi, H., Tate, J., Park, S., Park, C. H. & Keszler, D. A. p-Type conductivity in transparent oxychalcogenides. *Appl. Phys. Lett.* **82**, 2814 (2003).
12. Kiran, V., Mukherjee, D., Jenjeti, R. N. & Sampath, S. Active guests in the layered host of MoS2: Efficient visible light driven photocatalyst for hydrogen evolution. *Nanoscale* **6**, 12856 (2014).
13. Sheng, S., Fang, G., Li, C., Xu, S. & Zhao, X. p-type transparent conducting oxides. *Phys. Status Solidi (a)* **203** (8), 1891–1900 (2006).
14. Bouferrache, K. et al. Organic–inorganic hexahalometalate-crystal semiconductor K_2(Sn, Se, Te)Br_6 hybrid double perovskites for solar energy applications. *RSC Adv.* **15**, 11923–11933 (2025).
15. Scanlon, D. O., Walsh, A. & Watson, G. W. Understanding the p-type conduction properties of the transparent conducting oxide CuBO2: A density functional theory analysis. *Chem. Mater.* **21**, 4568 (2009).
16. Dixon, S. C., Scanlon, D. O., Carmalt, C. J. & Parkin, I. P. n-Type doped transparent conducting binary oxides: An overview. *J. Mater. Chem. C.* **4**, 6946 (2016).
17. Kumar, M. & Persson, C. Cu(Sb,Bi)(S,Se)2 as potential photovoltaic absorbers: Insights from theory. *Energy Procedia.* **44**, 176 (2014).
18. Jack, N. et al. ClarkeSynthesis, structure, and properties of the layered oxide chalcogenides $Sr_2CuO_2Cu_2S_2$ and $Sr_2CuO_2Cu_2Se_2$,. *Inorg. Chem.* **57** (24), 15379–15388 (2018).
19. Yanagi, H., Hase, T., Ibuki, S., Ueda, K. & Hosono, H. Bipolarity in electrical conduction of transparent oxide semiconductor $CuInO_2$ with delafossite structure. *Appl. Phys. Lett.* **78**, 1583 (2001).
20. Kamihara, Y. et al. Iron-based layered superconductor: LaOFeP. *J. Am. Chem. Soc.* **128**, 10012 (2006).
21. Wang, N. et al. Thermal transport and mechanical properties of layered oxychalcogenides LaCuOX (X = S,Se,Te). *ACS Appl. Energy Mater.* **5** (6), 6943–6951 (2022).
22. Jackson, A. J., Tiana, D. & Walsh, A. A universal chemical potential for sulfur vapours. *Chem. Sci.* **7**, 1082 (2016).
23. Hiramatsu, H. et al. Crystal structures, optoelectronic properties, and electronic structures of layered oxychalcogenides MCuOCh (M = Bi, La; Ch = S, Se, Te): Effects of electronic configurations of M3+ Ions. *Chem. Mater.* **20**, 326 (2008).
24. Tate, J. A., Platt, H. A. S. & Keszler, D. A. Combinatorial synthesis and optical characterization of wide band gap Cu-O-X (X = S, Se) thin films. *Thin Solid Films* **516**, 5795 (2008).
25. Scanlon, D. O. & Walsh, A. Bandgap engineering of $ZnSnP_2$ for high-efficiency solar cells. *Appl. Phys. Lett.* **100**, 251911 (2012).
26. Boudiaf, K. et al. Structural, elastic, electronic and optical properties of LaOAgS-type silver fluoride chalcogenides: First-principles study. *J. Electron. Mater.* **46**, 4539–4556 (2017).
27. Zakutayev, A. et al. Defect tolerant semiconductors for solar energy conversion. *J. Appl. Phys.* **107**, 103713 (2010).
28. Farrell, L. et al. Conducting mechanism in the epitaxial p-type transparent conducting oxide Cr_2O_3:Mg. *Phys. Rev. B.* **91**, 125202 (2015).
29. Ohta, H. et al. Highly electrically conductive indium–tin–oxide thin films epitaxially grown on yttria-stabilized zirconia (100) by pulsed-laser deposition. *Appl. Phys. Lett.* **76**, 2740 (2000).
30. Sallis, S. et al. Role of lone pair electrons in determining the optoelectronic properties of BiCuOSe. *Phys. Rev. B.* **85**, 085207 (2012).
31. Hiramatsu, H. et al. Degenerate p-type conductivity in wide-gap $LaCuOS_{1-x}Se_x$ (x = 0–1) epitaxial films. *Appl. Phys. Lett.* **91**, 012104 (2007).
32. Robertson, J. & Falabretti, B. Band offsets of high K gate oxides on III-V semiconductors. *J. Appl. Phys.* **100**, 014111 (2006).
33. Bellotti, E., Bertazzi, F. & Goano, M. Numerical analysis of HgCdTe simultaneous two-color photovoltaic infrared detectors. *J. Appl. Phys.* **105**, 053103 (2009).
34. Kumar, M., Umezawa, N., Zhou, W. & Imai, M. Defect induced room temperature ferromagnetism in single crystal, poly-crystal, and nanorod ZnO: A comparative study. *J. Mater. Chem. A.* **5**, 25293 (2017).
35. Zhan, F., Zhao, X. H., Xiao, W. Z., Liu, Y. & Ao, Z. M. Theoretical prediction of elastic stiffness and minimum lattice thermal conductivity of Y3Al5O12, YAlO3 and Y4Al2O9. *RSC Adv.* **5**, 48692 (2015).
36. Li, C., Li, Y. & Huang, Y. Anisotropic elastic properties of MB (M=Cr, Mo, W) monoborides: A first-principles investigation. *Phys. Chem. Chem. Phys.* **17**, 24003 (2015).
37. Dixon, S. C. et al. Transparent conducting n-type ZnO:Sc – synthesis, optoelectronic properties and theoretical insight. *J. Mater. Chem. C.* **5**, 7585 (2017).
38. Walsh, A., Payne, D. J., Egdell, R. G. & Watson, G. W. Stereochemistry of post-transition metal oxides: Revision of the classical lone pair model. *Chem. Soc. Rev.* **40**, 4455 (2011).
39. Tilley, R. J. D. *Perovskites: Structure-Property Relationships* (Wiley, 2016).
40. Kresse, G. & Furthmüller, J. Efficient iterative schemes for ab initio total-energy calculations using a plane-wave basis set. *Comput. Mater. Sci.* **6**, 15 (1996).
41. Perdew, J. P., Burke, K. & Ernzerhof, M. Generalized gradient approximation made simple. *Phys. Rev. Lett.* **77**, 3865 (1996).

42. Born, M. & Huang, K. *Dynamical Theory of Crystal Lattices* (Oxford University Press, 1954).
43. Zhou, Y. et al. Thin-film Sb2Se3 photovoltaics with oriented one-dimensional ribbons and benign grain boundaries. *Nat. Photonics*. **9**, 409 (2015).
44. Brandt, R. E., Stevanović, V., Ginley, D. S. & Buonassisi, T. Identifying defect-tolerant semiconductors with high minority-carrier lifetimes: Beyond hybrid lead halide perovskites. *MRS Commun.* **5**, 265 (2015).
45. Ishiwata, S. et al. Extremely high electron mobility in a phonon-glass semimetal. *Nat. Mater.* **12**, 512 (2013).
46. Yu, L. & Zunger, A. Identification of potential photovoltaic absorbers based on first-principles spectroscopic screening of materials. *Phys. Rev. Lett.* **108**, 068701 (2012).
47. Shockley, W. & Queisser, H. J. Detailed balance limit of efficiency of p-n junction solar cells. *J. Appl. Phys.* **32**, 510 (1961).
48. Green, M. A. Radiative efficiency of state-of-the-art photovoltaic cells. *Prog. Photovolt*. **20**, 472 (2012).
49. Gomes, L. C. & Carvalho, A. Phosphorene analogues: Isoelectronic two-dimensional group-IV monochalcogenides with orthorhombic structure. *Phys. Rev. B*. **92**, 085406 (2015).
50. Persson, C. Electronic and optical properties of Cu2ZnSnS4 and Cu2ZnSnSe4. *J. Appl. Phys.* **107**, 053710 (2010).
51. Kumar, M., Umezawa, N. & Imai, M. Magnetic and electronic properties of d0 semiconductors doped with Cu, Ag, or Au: A density functional study. *Phys. Chem. Chem. Phys.* **18**, 27930 (2016).
52. Hohenberg, P. & Kohn, W. *Inhomogeneous electron. gas Phys. Rev.* **136**, B864 (1964).
53. Kohn, W. & Sham, L. J. Self-consistent equations including exchange and correlation effects. *Phys. Rev.* **140**, A1133 (1965).
54. Martin, R. M. *Electronic Structure: Basic Theory and Practical Methods* (Cambridge University Press, 2004).
55. Blaha, P. et al. *L. D. Marks, WIEN2k: An Augmented Plane Wave Plus Local Orbitals Program for Calculating Crystal Properties* (Vienna University of Technology, 2018).
56. Schwarz, K., Blaha, P. & Madsen, G. K. H. Electronic structure calculations of solids using the WIEN2k package for material sciences. *Comput. Phys. Commun.* **147**, 71 (2002).
57. Singh, D. J. & Nordstrom, L. *Planewaves, Pseudopotentials, and the LAPW Method* 2nd edn (Springer, 2006).
58. Anisimov, V. I., Aryasetiawan, F. & Lichtenstein, A. I. First-principles calculations of the electronic structure and spectra of strongly correlated systems: The LDA+U method. *J. Phys.: Condens. Matter*. **9**, 767 (1997).
59. Dudarev, S. L., Botton, G. A., Savrasov, S. Y., Humphreys, C. J. & Sutton, A. P. Electron-energy-loss spectra and the structural stability of nickel oxide: An LSDA+U study. *Phys. Rev. B*. **57**, 1505 (1998).
60. Heyd, J., Scuseria, G. E. & Ernzerhof, M. Hybrid functionals based on a screened Coulomb potential. *J. Chem. Phys.* **118**, 8207 (2003).
61. Ambrosch-Draxl, C. & Sofo, J. O. Linear optical properties of solids within the full-potential linearized augmented planewave method. *Comput. Phys. Commun.* **175**, 1 (2006).
62. Gajdoš, M., Hummer, K., Kresse, G., Furthmüller, J. & Bechstedt, F. Linear optical properties in the projector-augmented wave methodology. *Phys. Rev. B*. **73**, 045112 (2006).
63. Yu, P. Y. & Cardona, M. *Fundamentals of Semiconductors: Physics and Materials Properties* 4th edn (Springer, 2010).
64. Scheer, R. & Schock, H. W. *Chalcogenide Photovoltaics: Physics, Technologies, and Thin Film Devices* (Wiley-VCH, 2011).
65. Adachi, S. *Optical Properties of Crystalline and Amorphous Semiconductors: Materials and Fundamental Principles* (Springer, 1999).
66. Wooten, F. *Optical Properties of Solids* (Academic Press, 1972).
67. Togo, A. & Tanaka, I. First principles phonon calculations in materials science. *Scr. Mater.* **108**, 1 (2015).
68. Grimvall, G. *Thermophysical Properties of Materials* (Elsevier, 1999).
69. Otero-de-la-Roza, A., Abbasi-Pérez, D. & Luaña, V. Gibbs2: A new version of the quasiharmonic model code. II. Models for solid-state thermodynamics, features and implementation. *Comput. Phys. Commun.* **182**, 2232 (2011).
70. Gonze, X. & Lee, C. Dynamical matrices, Born effective charges, dielectric permittivity tensors, and interatomic force constants from density-functional perturbation theory. *Phys. Rev. B*. **55**, 10355 (1997).
71. Baroni, S., de Gironcoli, S., Dal Corso, A. & Giannozzi, P. Phonons and related crystal properties from density-functional perturbation theory. *Rev. Mod. Phys.* **73**, 515 (2001).
72. Parlinski, K., Li, Z. Q. & Kawazoe, Y. First-principles determination of the soft mode in cubic ZrO2. *Phys. Rev. Lett.* **78**, 4063 (1997).
73. Leibfried, G. & Ludwig, W. Theory of anharmonic effects in crystals. *Solid State Phys.* **12**, 275 (1961).
74. Maradudin, A. A., Montroll, E. W., Weiss, G. H. & Ipatova, I. P. *Theory of Lattice Dynamics in the Harmonic Approximation (*Academic Press, 1971).
75. Kunc, K. & Martin, R. M. Ab initio force constants of GAAS: A new approach to calculation of phonons and dielectric properties. *Phys. Rev. Lett.* **48**, 406 (1982).
76. Singh, D. J. *Planewaves, Pseudopotentials, and the LAPW Method* (Kluwer Academic, 1994).
77. Blaha, P., Schwarz, K., Madsen, G. K. H., Kvasnicka, D. & Luitz, J. *WIEN2k, An Augmented Plane Wave + Local Orbitals Program for Calculating Crystal Properties, Karlheinz Schwarz, Techn* (Universität Wien, 2001).
78. Birch, F. Finite elastic strain of cubic crystals. *Phys. Rev.* **71**, 809 (1947).
79. Perdew, J. P. & Wang, Y. Accurate and simple analytic representation of the electron-gas correlation energy. *Phys. Rev. B*. **45**, 13244 (1992).
80. Liechtenstein, A. I., Anisimov, V. I. & Zaanen, J. Density-functional theory and strong interactions: Orbital ordering in Mott-Hubbard insulators. *Phys. Rev. B*. **52**, R5467 (1995).
81. Jiang, M. et al. The origin of incipient ferroelectricity in lead telluride. *Phys. Rev. Lett*. **110**, 185701 (2013).
82. Monkhorst, H. J. & Pack, J. D. Special points for Brillouin-zone integrations. *Phys. Rev. B*. **13**, 5188 (1976).
83. Hill, R. The elastic behaviour of a crystalline aggregate. *Proc. Phys. Soc. A*. **65**, 349 (1952).
84. Voigt, W. *Lehrbuch der Kristallphysik* (Teubner, 1928).
85. Reuss, A. Berechnung der Fließgrenze von Mischkristallen auf Grund der Plastizitätsbedingung für Einkristalle. *Z. für Angewandte Math. und Mechanik*. **9**, 49 (1929).
86. Dresselhaus, M. S., Dresselhaus, G. & Jorio, A. *Group Theory: Application to the Physics of Condensed Matter* (Springer, 2008).
87. Baroni, S., Giannozzi, P. & Testa, A. Green's-function approach to linear response in solids. *Phys. Rev. Lett.* **58**, 1861 (1987).
88. Parlinski, K. et al. *Software Phonon, Cracow, Poland*. First-principles investigation of structurlectronic, mechanical, optical, and thermodynamic properties of novel quaternary oxychalcogenide LaCuTeO for optoelectronic applications (2003).
89. Gul, B., Abdullah, S., Alharbi, R., Khan, M. S. & MaisarahAziz, S. Chalcogen-mediated band tuning, optoelectronic and transport properties of LaCuXO (X = Se, Te) Oxychalcogenides: First-principles study. *Chem. Phys. Lett.* **878**, 142248 (2025).
90. Raj Natarajan, A. et al. High thermoelectric performance of layered LaAgXO (X=Se,Te) from electrical and thermal transport calculations. *Phys. Rev. Mater.* **7**, 025405 (2023).
91. Woods-Robinson, R. et al. Wide band gap chalcogenide semiconductors. *Chem. Rev.* **120** (9), 4007–4055 (2020).

Acknowledgements

The authors are thankful to the Deanship of Graduate Studies and Scientific Research at Najran University for funding this work under the Elite Funding Program grant code (NU/EP/SERC/14/4228-2).

Author contributions

Conceptualization: Elkenany Brens Elkenany, Murat YaylacıData curation: Hasan B. Albargi, Aseel Smerat, Ramzi Dhahri, (A) M. Abdelghany Formal analysis and validation : (B) Ghebouli.

Declarations

Competing interests

The authors declare no competing interests.

Additional information

Correspondence and requests for materials should be addressed to E.B.E.

Reprints and permissions information is available at www.nature.com/reprints.

Publisher's note Springer Nature remains neutral with regard to jurisdictional claims in published maps and institutional affiliations.

Open Access This article is licensed under a Creative Commons Attribution-NonCommercial-NoDerivatives 4.0 International License, which permits any non-commercial use, sharing, distribution and reproduction in any medium or format, as long as you give appropriate credit to the original author(s) and the source, provide a link to the Creative Commons licence, and indicate if you modified the licensed material. You do not have permission under this licence to share adapted material derived from this article or parts of it. The images or other third party material in this article are included in the article's Creative Commons licence, unless indicated otherwise in a credit line to the material. If material is not included in the article's Creative Commons licence and your intended use is not permitted by statutory regulation or exceeds the permitted use, you will need to obtain permission directly from the copyright holder. To view a copy of this licence, visit http://creativecommons.org/licenses/by-nc-nd/4.0/.

© The Author(s) 2026